

# A Low-Temperature Annealing Method for Alloy Nanostructures and Metasurfaces: Unlocking a Novel Degree of Freedom

Debdatta Ray, Hsiang-Chu Wang, Jeonghyeon Kim, Christian Santschi, and Olivier J. F. Martin\*

The material and exact shape of a nanostructure determine its optical response, which is especially strong for plasmonic metals. Unfortunately, only a few plasmonic metals are available, which limits the spectral range where these strong optical effects can be utilized. Alloying different plasmonic metals can overcome this limitation, at the expense of using a high-temperature alloying process, which adversely destroys the nanostructure shape. Here, a low-temperature alloying process is developed where the sample is heated at only 300 °C for 8 h followed by 30 min at 450 °C and Au–Ag nanostructures with a broad diversity of shapes, aspect ratios, and stoichiometries are fabricated. Energy-dispersive X-ray spectroscopy and X-ray photoelectron spectroscopy analyses confirm the homogeneous alloying through the entire sample. Varying the alloy stoichiometry tunes the optical response and controls spectral features, such as Fano resonances. Binary metasurfaces that combine nanostructures with different stoichiometries are fabricated using multiple-step electron-beam lithography, and their optical function as a hologram or a Fresnel zone plate is demonstrated at the visible wavelength of  $\lambda = 532$  nm. This low-temperature annealing technique provides a versatile and cost-effective way of fabricating complex Au–Ag nanostructures with arbitrary stoichiometry.

## 1. Introduction

Every nanotechnology is indissociable from the materials it uses. Conversely, the materials involved often determine and limit the possible technological choices and the potential applications that can be envisioned. This is true for many different

scientific fields, from energy<sup>[1,2]</sup> to chemistry,<sup>[3,4]</sup> semiconductors,<sup>[5–7]</sup> medicine,<sup>[8,9]</sup> or even food industry.<sup>[10]</sup> Plasmonics—the resonant optical interaction of light with free electrons in metals—also strongly relies on the utilization of specific materials, viz., coinage metals with a very high free electron density.<sup>[11]</sup>


Thanks to its electronic properties, ease of fabrication and chemical stability, gold (Au) is the most widely used coinage metal for plasmonic applications. Its dielectric function  $\epsilon(\lambda)$ , where  $\lambda$  is the wavelength of light, produces a plasmon resonance in the long-wavelength range of the visible spectrum. Other metals, like aluminum (Al) and silver (Ag), have plasmon resonances toward shorter wavelengths, but are more difficult for nanotechnology.<sup>[12]</sup> While the real part of  $\epsilon(\lambda)$  determines the wavelength at which the plasmon resonance occurs, its imaginary part controls the plasmon resonance strength.<sup>[13]</sup> Since a decade, there has been a surge of research for alternative materials to Au, Ag, and Al,

in order to exploit plasmon resonances over the entire visible and near infrared spectrum.<sup>[14–16]</sup>

In addition to pure materials, heterogeneous combinations of metals, such as core–shell particles<sup>[17]</sup> and alloys<sup>[18]</sup> have also been proposed. Especially Au–Ag alloys have demonstrated extremely interesting properties in terms of dielectric function tunability and chemical stability.<sup>[19,20]</sup> The capability of alloys to adjust the optical properties of the individual metals by altering their electronic band structure,<sup>[18,21–23]</sup> is the driving force behind a large number of applications, including surface enhanced Raman spectroscopy,<sup>[19,20,24–26]</sup> biosensing,<sup>[27–30]</sup> therapeutics,<sup>[21]</sup> photochemistry,<sup>[31–33]</sup> color generation,<sup>[34]</sup> and generation of hot electrons.<sup>[35]</sup> Moreover, Au–Ag alloys are chemically more stable than pure Ag<sup>[19]</sup> and Au–Ag alloy very well thanks to their similar lattice constants<sup>[36]</sup> and a very simple binary phase diagram.<sup>[37]</sup>

Existing techniques for the fabrication of Au–Ag alloys include laser ablation,<sup>[38]</sup> coreduction of Au–Ag salts,<sup>[39,40]</sup> codeposition,<sup>[41,42]</sup> annealing at very high temperatures of Au–Ag core–shell nanoparticles with<sup>[43–45]</sup> and without<sup>[46]</sup> SiO<sub>2</sub> coating. All those bottom-up techniques provide limited control

D. Ray, H.-C. Wang, J. Kim, C. Santschi, O. J. F. Martin  
Nanophotonics and Metrology Laboratory  
Swiss Federal Institute of Technology  
Lausanne (EPFL), Lausanne 1015, Switzerland  
E-mail: olivier.martin@epfl.ch

 The ORCID identification number(s) for the author(s) of this article can be found under <https://doi.org/10.1002/adma.202108225>.

© 2022 The Authors. Advanced Materials published by Wiley-VCH GmbH. This is an open access article under the terms of the Creative Commons Attribution-NonCommercial-NoDerivs License, which permits use and distribution in any medium, provided the original work is properly cited, the use is non-commercial and no modifications or adaptations are made.

DOI: 10.1002/adma.202108225

of the nanoparticles shape, stoichiometry, as well as its reproducibility. In contrast, top-down fabrication techniques, such as e-beam lithography (EBL), are remarkably versatile and provide reliable control over the shape and size of individual nanoparticles.<sup>[47]</sup> Since the size of targeted nanostructures is typically in the range of a few tens to hundreds of nm, metal depositions are carried out using directional e-beam evaporation rather than isotropic cosputtering to ensure reliable lift-off performances. Alloys have been deposited either by alloyed targets,<sup>[48]</sup> which is costly since each stoichiometry requires a different target; or by alternating deposition of thin Au and Ag layers with subsequent annealing at high temperature, resulting in nanostructures that do not retain the original shape.<sup>[49]</sup> This represents a very severe limitation since the shape of plasmonic nanostructures determines their optical properties.<sup>[13]</sup> This warrants a need for cost-effective techniques for the stable fabrication of alloyed nanostructures with well-controlled sizes and shapes.

Here, we address this challenge and propose an original process for fabricating alloyed nanostructures. The method is based on the deposition of a bilayer of Au and Ag with subsequent annealing at low temperature at 300 °C, far below the melting points of the individual metals. Thanks to the low temperature, the shape of the nanoparticles is retained after annealing. To demonstrate and verify that homogeneous alloys can be fabricated by this low-temperature process, we first fabricate thin films of Au–Ag alloys and confirm their homogeneity by X-ray photoelectron spectroscopy (XPS) and energy-dispersive X-ray spectroscopy (EDX). Ellipsometric studies demonstrate the variation of the permittivity across different compositions. This technique is then applied to fabricate different alloyed nanostructures that perfectly retain their shape after low-temperature annealing. Optical measurements demonstrate that the dielectric function of these nanostructures is tuned by varying the alloy's composition. Finally, metasurfaces that combined different alloys are realized and their optical function as hologram or Fresnel zone plate is demonstrated experimentally in the visible part of the spectrum.

## 2. Alloyed Thin Films

Au–Ag nanostructures are normally alloyed at temperatures in the order of 800–900 °C, close to the melting point of the metals.<sup>[22,44,50]</sup> To demonstrate as a first step the successful annealing at a temperature as low as 300 °C, thin Au–Ag films are fabricated, as described in **Figure 1a**. The total film thickness is 150 nm and is kept constant for the different compositions. The latter are determined by depositing different thicknesses of Au and Ag using the e-beam evaporator LAB600H (Leybold-Optics).

To illustrate this process, let us consider the fabrication of an Au<sub>0.2</sub>Ag<sub>0.8</sub> alloy: 120 nm of Ag first, followed by 30 nm of Au are deposited on a float glass substrate coated with 2 nm of Ti acting as an adhesion layer. Immediately afterward, the entire film is annealed under N<sub>2</sub> atmosphere in an oven (Neytech Qex Vacuum Porcelain furnace) at 300 °C for 8 h followed by 30 min at 450 °C. Trial and error has demonstrated that this additional 30 min annealing at 450 °C homogenizes the alloy: XPS results for a 150 nm Au<sub>0.2</sub>Ag<sub>0.8</sub> film annealed

only at 300 °C for 8 h without this additional step indicate that the film is inhomogeneous, **Figure S1a** (Supporting Information). This short higher temperature step appears to be the maximum nanostructures can endure without deformation, as discussed in **Figure S2** (Supporting Information). **Figure 1b,c** shows scanning electron microscopy (SEM) images for this double layer film before and after annealing (300 °C for 8 h followed by 30 min at 450 °C), with insets providing magnified views. It can be clearly seen that the film has lost its grainy appearance and reorganized into a more crystalline configuration during the annealing process.<sup>[51,52]</sup> EDX maps of all elements of interest are superimposed in **Figure 1d**, revealing a homogeneous distribution of Au and Ag. XPS analysis demonstrates a homogeneous alloy over the entire 150 nm depth, **Figure 1e**. In contrast, XPS analysis of films carried out prior to annealing distinctly shows the bilayer of Ag and Au, **Figure S1b** (Supporting Information). Thus, XPS and EDX results confirm that we have a homogeneous Au–Ag distribution after annealing the samples at low temperature, even for a relatively thick film. **Figure 1f** reports the experimentally obtained ellipsometric data for Au, Au<sub>0.2</sub>Ag<sub>0.8</sub>, Au<sub>0.5</sub>Ag<sub>0.5</sub>, and Ag. It can be seen that the real part of the dielectric function for both alloys lies between pure Au and pure Ag. This modification of  $\epsilon_{\text{real}}$  with change in composition leads to variations of the plasma frequency as well.<sup>[53]</sup> The imaginary part, however, is more complicated since it reflects the material losses and can be affected by various factors, such as grain boundaries and defect sites.<sup>[54,55]</sup> Ellipsometry and numerical analysis were carried out using SOPRA GES 5E and WINELI II software, respectively. For all the measurements, the incident angle was kept at 75° and both real and imaginary parts of the dielectric function were extracted from the amplitude component  $\Phi$  and the phase difference  $\Delta$ .<sup>[12]</sup> The experimental data are compared in **Figure S3** (Supporting Information) with the permittivity model of Rioux et al.,<sup>[56]</sup> which agrees very well. The experimental data agree also well with the experimental values reported by Rodriguez et al.<sup>[57]</sup> All these data are available in the open dataset associated with this publication.<sup>[58]</sup> Thin films both before and after alloying exhibit some roughness, as indicated by the atomic force microscopy (AFM) measurements in **Figure S4** (Supporting Information). The roughness standard deviation remains in the order of 2 nm for both cases, while the surface waviness increases after annealing, indicative of larger grains. It should be emphasized that the roughness on the top surface of a plasmonic nanostructure barely influences its response, since the free electrons in the metal oscillate in the plane of the structure.<sup>[59]</sup>

Before we proceed to more results, we would like to briefly discuss the conditions that make alloying at low temperature successful. Homogeneously alloyed samples at 300 °C—which is well below the Tamman temperature of Au and Ag<sup>[60]</sup>—require the annealing to be performed within a few days after metal deposition. The deposition of the metal film, leaves it in an unstable morphology due to the presence of high relative humidity and the film remains in this state for a couple of days after the deposition.<sup>[51]</sup> Since the film is not yet well-ordered, it takes less thermal energy for the Au and Ag atoms to diffuse. Thus, the onset of the diffusion occurs at lower temperatures, which makes it possible to completely alloy thin

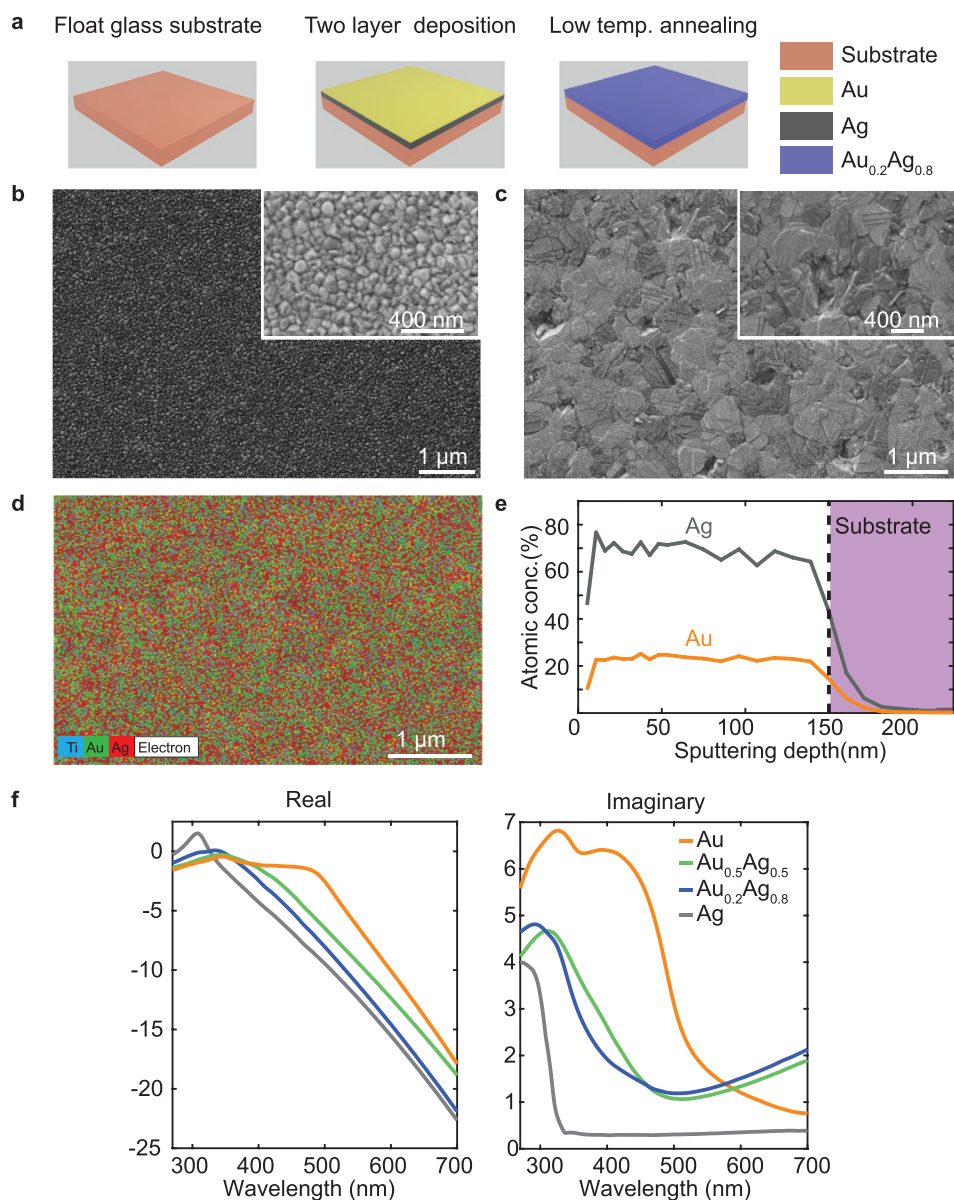


**Figure 1.** Demonstration of low-temperature alloyed thin films. a) Process flow for fabricating thin films with a specific stoichiometry determined by the thicknesses of the different metal layers. b) SEM image of a double-layer film for  $\text{Au}_{0.2}\text{Ag}_{0.8}$  before annealing. c) SEM image of the same film after annealing. The insets in (b) and (c) show a magnified view. d) Superimposed EDX maps for Au, Ag, and Ti. e) XPS analysis of the  $\text{Au}_{0.2}\text{Ag}_{0.8}$  alloy, demonstrating a homogeneous alloy over the entire 150 nm depth. f) Experimentally obtained ellipsometric data for pure Au,  $\text{Au}_{0.2}\text{Ag}_{0.8}$ ,  $\text{Au}_{0.5}\text{Ag}_{0.5}$ , and pure Ag.

films at a temperature of 300 °C. On the other hand, we have observed that it was not possible to anneal at low temperature any bilayer Au–Ag films that were kept in a nitrogen atmosphere (Saito Keiryoki MFG. CO. LTD) for more than a week before annealing. This is shown in Figure S5 (Supporting Information), with SEM images before and after annealing for 150 nm  $\text{Au}_{0.8}\text{Ag}_{0.2}$  thin films kept in nitrogen atmosphere for 4.5 months after deposition. After annealing, nanoparticles are formed on the film (Figure S5d, Supporting Information), as opposed to a homogeneous alloyed film that was obtained when annealed within a few days of deposition (Figure S5b, Supporting Information). Moreover, the appearance of the

not-annealed bilayer film after 4.5 months is very different (more smooth and flat, Figure S5c, Supporting Information) compared to that after only a few days (more grainy, Figure S5a, Supporting Information). This indicates that with passing time the bilayer film becomes very stable and thus requires a higher temperature to form an homogeneous alloy.

Au–Ag alloys are of paramount importance thanks to their optical and chemical properties, and remain the focus of this work. Yet, we would like to mention that it is likely that a similar approach could be used to alloy other metals at low temperature, like for example Au–Pd, see Figure S6 (Supporting Information).

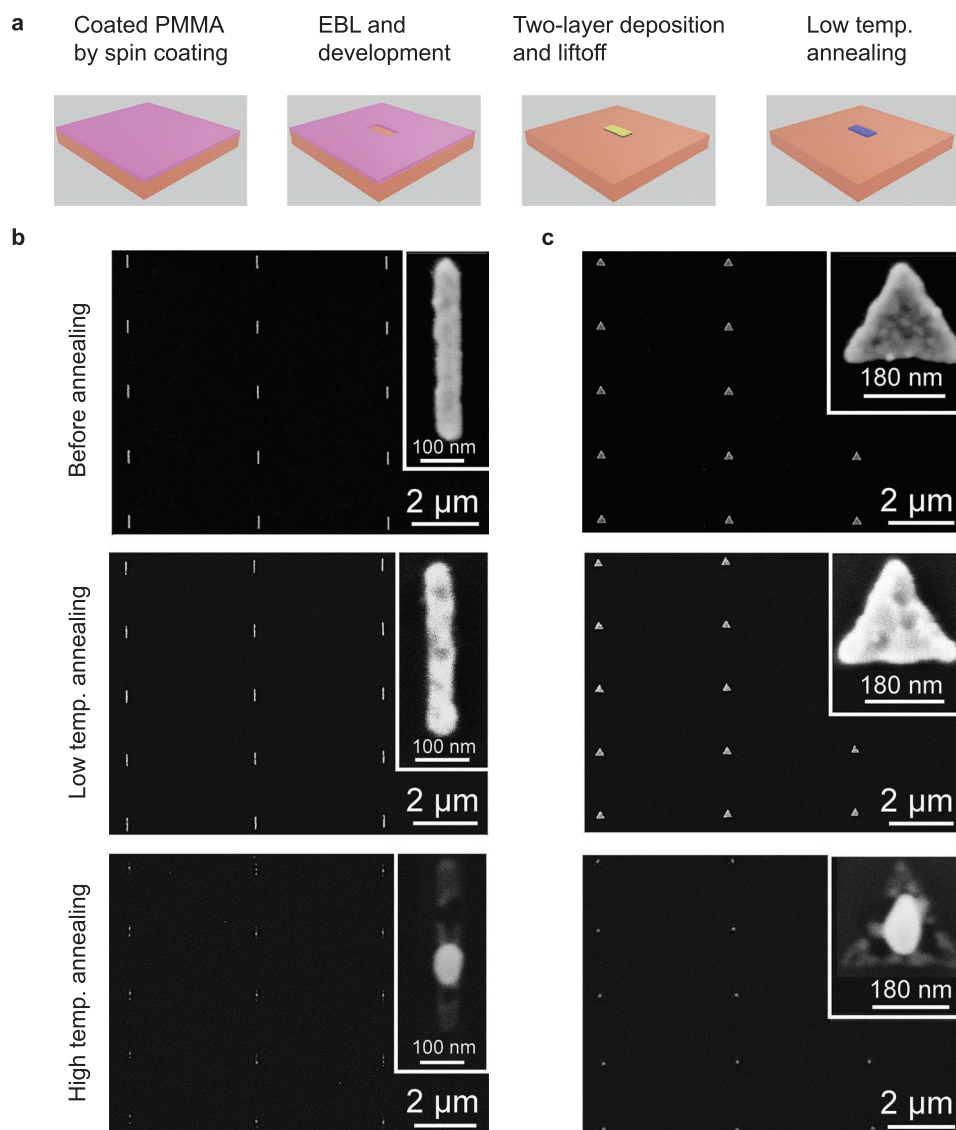


**Figure 2.** Fabrication and optical characterization of alloyed nanostructures. a) Process flow (same colors as in Figure 1a). b,c) SEM images of an array of  $\text{Au}_{0.2}\text{Ag}_{0.8}$   $400 \times 50 \text{ nm}^2$  rods (b) and  $260 \text{ nm}$  equilateral triangles (c) before (top row) and after low-temperature annealing at  $300 \text{ }^\circ\text{C}$  for 8 h followed by  $450 \text{ }^\circ\text{C}$  for 30 min (middle row), as well as high-temperature annealing at  $800 \text{ }^\circ\text{C}$  for 3 h (bottom row). The insets show a single nanostructure from the corresponding array.

### 3. Alloyed Nanostructures

The advantages associated with the low-temperature annealing presented in this article are unleashed for the fabrication of nanostructures with different stoichiometries, as illustrated in Figure 2a. Similar to the alloyed thin films the Au–Ag bilayers are deposited by e-beam evaporation. Figure 2b,c shows SEM images of an array of  $50 \text{ nm}$  thick rods and triangles before and after annealing. The corresponding insets magnify a single  $400 \times 50 \text{ nm}^2$  nanorod and a nanotriangle with a  $260 \text{ nm}$  side length. It is remarkable that the nanostructure shapes are perfectly retained after annealing, even for structures with a very high aspect ratio. The yield of this approach is also very high, as indicated by the widefield images. EDX measurements shown in Figure S7 (Supporting Information) reveal a homogeneous

Au–Ag distribution over the entire nanostructure. The benefits of the low-temperature annealing process can be better appreciated by looking at the SEM images for similar nanostructures obtained by high-temperature annealing at  $800 \text{ }^\circ\text{C}$  for 3 h in a nitrogen environment (bottom row of Figure 2b,c). Those nanostructures do not retain their shape at all, as opposed to those of low-temperature annealing. Consequently, nanostructures with a specific shape, annealed at high temperature will not exhibit the optical response for which they were designed.<sup>[61]</sup>

More sophisticated arrangements like 4-rod Fano-resonant structures are fabricated,<sup>[51,62]</sup> Figure 3a. The lengths of the longer and shorter rods are  $130$  and  $68 \text{ nm}$ , respectively. The gaps are  $30 \text{ nm}$  and the structures thickness is  $40 \text{ nm}$ . After annealing, the shape is perfectly retained. The Fano spectrum arises from the interference of a broad bright and narrow dark

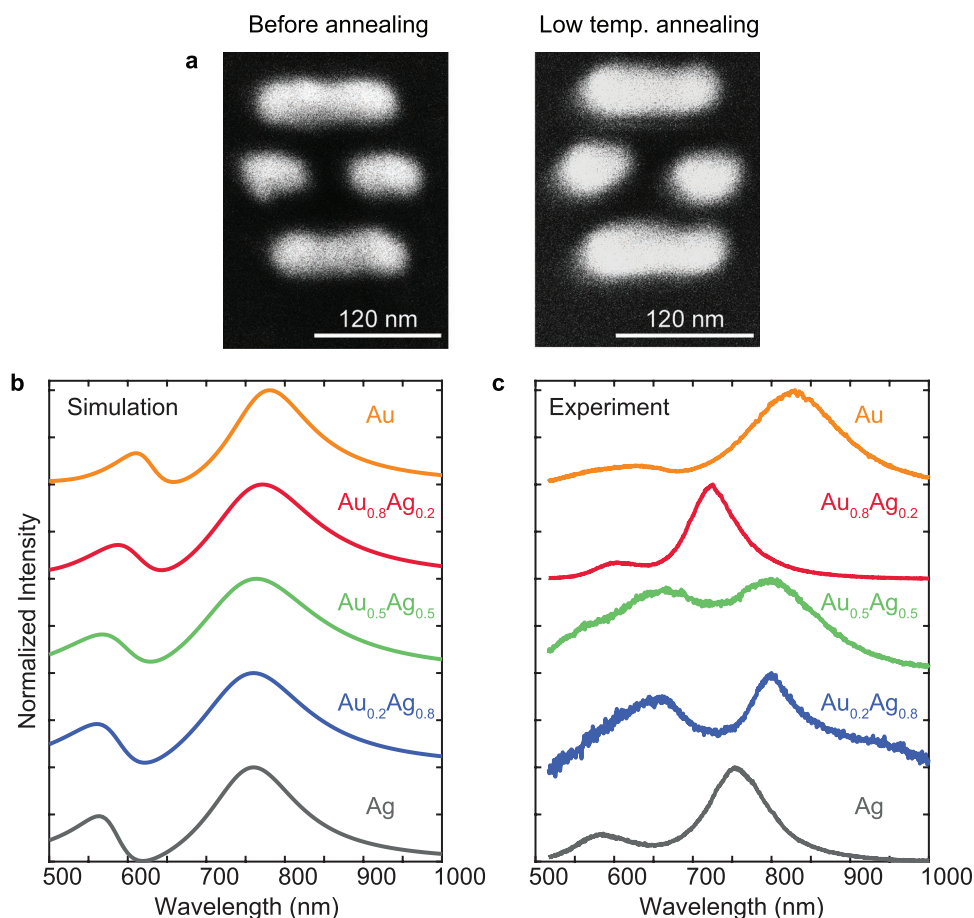


**Figure 3.** Fabrication and optical characterization of Fano resonant structures. a) SEM images of a  $\text{Au}_{0.8}\text{Ag}_{0.2}$  4-rod Fano-resonant structure before and after low-temperature annealing. b) Calculated and c) measured optical reflectance spectra of the Fano-resonant structures with different stoichiometries.

mode<sup>[62]</sup> and can be tuned by changing the alloy composition. Exactly the same geometry was fabricated in 5 different stoichiometries: Au,  $\text{Au}_{0.8}\text{Ag}_{0.2}$ ,  $\text{Au}_{0.5}\text{Ag}_{0.5}$ ,  $\text{Au}_{0.2}\text{Ag}_{0.8}$ , and Ag. The reflectance of these structures measured in dark field microscope (setup described in Figure S8, Supporting Information) are shown in Figure 3c. The experiments confirm the variation of the spectra with the composition. Simulations were carried out using the surface integral equation method<sup>[63,64]</sup> and the dielectric functions obtained from the Rioux model.<sup>[56]</sup> At first sight, the agreement between simulations and experiments is fair. A more in-depth analysis performed on several different samples using the extended coupled oscillator model (ECO),<sup>[62]</sup> is reported in Figure S9 (Supporting Information). Briefly, the ECO model includes one oscillator for the diabatic mode DA supported by the dipole antenna in the center of the structure, and one oscillator for the diabatic mode DN supported by the two outer nanostructures, Figure 3a. The agreement between measurements and simulations is good for the DA resonance frequency, while it is poor for the DN resonance frequency, Figure S9 (Supporting Information). This indicates that those outer nanostructures are displaced with respect to the numerical model. The results presented in this section demonstrate the additional degree of freedom offered

by the fabrication of alloyed Au–Ag nanostructures with varying stoichiometry.

EBL is used here as a proof of concept and this alloying technique is compatible with other nanotechnologies, including for example colloidal lithography,<sup>[65]</sup> which can be used to produce nanostructures over a large area.

#### 4. Alloyed Metasurfaces

Let us now apply this low-temperature annealing technique to the fabrication of metasurfaces like holograms and Fresnel zone plates, which require combining alloyed nanostructures with different stoichiometries on the same substrate. Generally, tuning the response of a meta-atom is achieved by tailoring its geometry to produce the desired phase and amplitude response.<sup>[66]</sup> Here, instead of varying the shape, we change the material while keeping the shape constant. Binary-phase metasurfaces are fabricated with two different alloys,  $\text{Au}_{0.8}\text{Ag}_{0.2}$  and  $\text{Au}_{0.2}\text{Ag}_{0.8}$ . It should be noted that in this work the meta-atoms shape is kept constant to emphasize the effect of changing the optical properties of the material; this nanotechnology can of course be applied to meta-atoms with different shapes as well

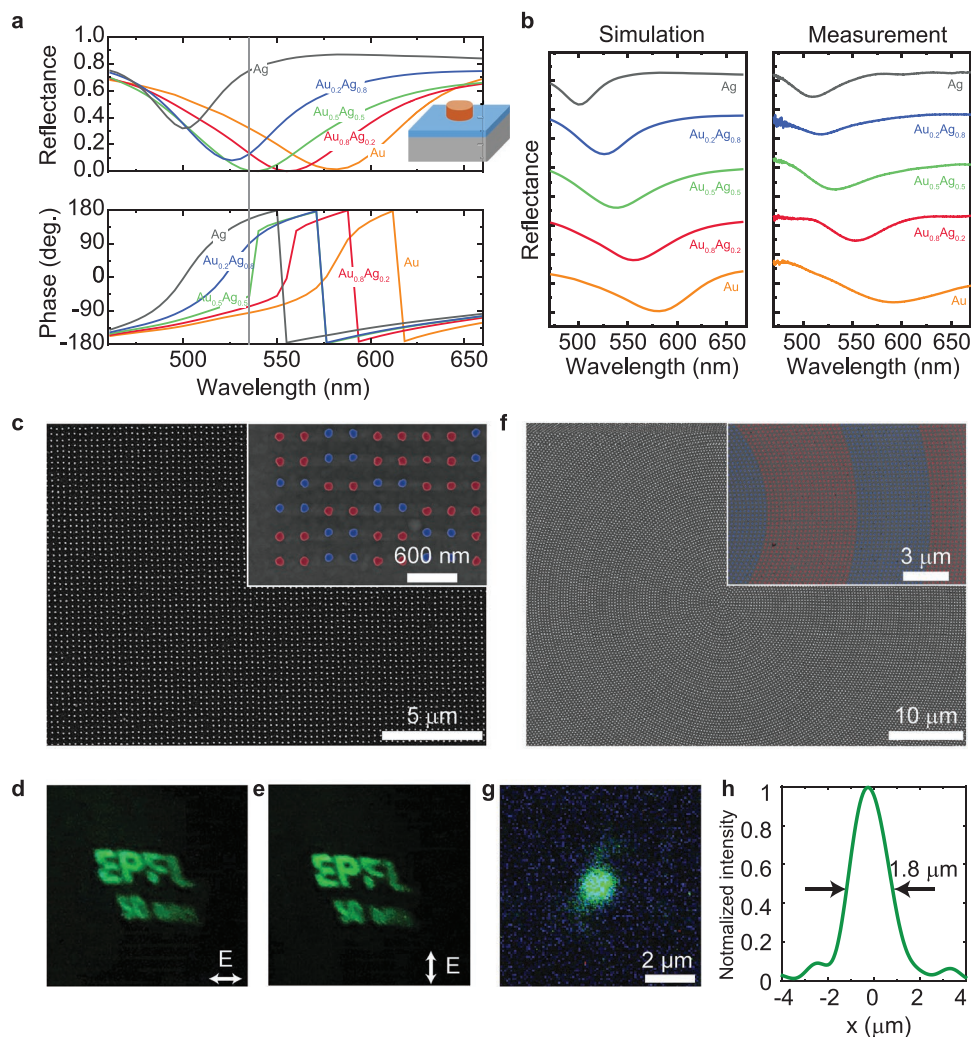


**Figure 4.** Alloyed metasurfaces. a) Simulated reflectance and phase for alloyed meta-atoms with different stoichiometries. The inset shows the meta-atom composed of an alloyed disc with diameter  $d = 110$  nm, height  $h = 50$  nm, positioned atop an Al mirror with a SiO<sub>2</sub> spacer of thickness  $t = 100$  nm. The period is  $p = 300$  nm. b) Simulated and measured reflectance spectra for different disc stoichiometries. c) SEM image of the hologram device and d, e) its optical projection under horizontally (d) and vertically (e) polarized light. f) SEM image of the FZP with focal length  $f = 400$  μm and NA = 0.35. g) Intensity distribution at the focal plane and h) normalized intensity profile at the center of the focal spot. The insets in (c) and (f) emphasize with colors the two different stoichiometries used for the meta-atoms.

as different stoichiometries, thus providing a very large number of degrees of freedom for the metasurface design.

With Au–Ag alloys, it is straightforward to develop metasurfaces that operate in the visible; here we chose  $\lambda = 532$  nm and fabricate a periodic array of meta-atoms with periodicity  $p = 300$  nm to avoid any diffraction order. Alloyed discs Au <sub>$x$</sub> Ag <sub>$1-x$</sub>  with diameter  $d = 110$  nm and thickness  $h = 50$  nm, atop an Al mirror (thickness 150 nm) with a  $t = 100$  nm thick SiO<sub>2</sub> spacer are used as meta-atoms, see the inset in Figure 4a. Such a structure is polarization insensitive and supports a gap plasmon,<sup>[67,68]</sup> which enables the reradiation of the incident wave with a phase shift that can be controlled over a  $2\pi$ -range.<sup>[69]</sup> The reflectance and phase shift are computed as a function of the wavelength using the periodic surface integral equation method,<sup>[63,64]</sup> Figure 4a. The permittivity for Al and SiO<sub>2</sub> originate from the literature,<sup>[70]</sup> whereas that for Au <sub>$x$</sub> Ag <sub>$1-x$</sub>  are computed using Rioux's model.<sup>[56]</sup> Figure 4a indicates that at  $\lambda = 532$  nm the

reflectance is the same for Au<sub>0.2</sub>Ag<sub>0.8</sub> and Au<sub>0.8</sub>Ag<sub>0.2</sub> nanostructures, while the phase they produce is shifted by 165°; this nanostructures pair can therefore serve as meta-atoms for a binary metasurface.<sup>[71]</sup> This is confirmed in Figure 4b by measurements on alloyed disc arrays with five different stoichiometries (reflectance measurement setup described in Figure S10, Supporting Information). The agreement between these measurements and simulations is good, especially the spectral locations of the reflection dip agree very well.

Having demonstrated the ability to manipulate the reflected light using arrays of alloyed nanostructures, let us now fabricate a meta-hologram and a Fresnel zone plate using the stoichiometries Au<sub>0.8</sub>Ag<sub>0.2</sub> and Au<sub>0.2</sub>Ag<sub>0.8</sub> to realize the two different disc-shaped meta-atoms. For the meta-hologram, we calculate the phase distribution using the computer generated hologram method.<sup>[72]</sup> Since the meta-hologram is built from two different alloys, a 3-step EBL process illustrated in

Figure S11 (Supporting Information) is required to position the corresponding nanostructures with different compositions on the metasurface. In the first step, alignment marks are written and in the consecutive 2nd, respectively 3rd steps, nanostructures with Au<sub>0.8</sub>Ag<sub>0.2</sub>, respectively Au<sub>0.2</sub>Ag<sub>0.8</sub>, are deposited. A position accuracy in the order of 20 nm is achieved thanks to the alignment markers. The annealing is performed after the final step, once all the meta-atoms with different stoichiometries have been deposited on the surface. The SEM images of the hologram device in Figure 4c indicate that all the unit cells share the same physical dimensions and the different meta-atoms are well aligned over a very large area (the inset highlights with colors the two different stoichiometries used in the metasurface). This is quite remarkable since these nanostructures are written in two successive, independent steps, including electron-beam resist coating, EBL, development, two-layer metal deposition and lift-off. Images of the hologram projection under polarized laser illumination are shown in Figure 4d,e for two different incident polarizations (setup described in Figure S12, Supporting Information). The holograms are polarization-independent thanks to the symmetrical arrangement of the meta-atoms.

For the Fresnel zone plate, the spatial phase profile follows the equation

$$\varphi(r) = \frac{2\pi}{\lambda} \left( \sqrt{r^2 + f^2} - f \right) \quad (1)$$

where  $r$  is the distance from the center of the lens and  $f$  represents the focal length.<sup>[73]</sup> For demonstration purposes, the lens is designed with a NA = 0.35 in air. The lens diameter is  $D = 300 \mu\text{m}$  and the focal length is  $f = 400 \mu\text{m}$ . Figure 4f shows the SEM image of the fabricated lens. The inset in Figure 4f provides a magnified view of the center part of the lens, which is composed of meta-atoms with the same dimensions but different Au–Ag stoichiometries. The focal spot, displayed in Figure 4g, is measured in the Fourier plane, whereas the intensity profile, shown in Figure 4h, is determined in the focal plane using the setup shown in Figure S13 (Supporting Information). The full width at half maximum (FWHM) is  $1.8 \mu\text{m}$ , which agrees extremely well with the theoretical diffraction spot size  $D_{\text{FWHM}} = 1.22 \lambda/\text{NA} = 1.85 \mu\text{m}$ .

One may consider that metasurfaces built from bilayer meta-atoms instead of alloyed meta-atoms could provide the same optical functions. While this is in principle possible, the design becomes more complicated since the mere metal deposition order has a strong influence on the optical response, Figure S14 (Supporting Information). Furthermore, in the case of a bilayer, the response shifts in a rather intricate manner as a function of the wavelength.

In addition to representing a disruptive approach to the design of optical metasurfaces, the utilization of alloyed nanostructures brings its own advantages compared to metasurfaces designed from a collection of meta-atoms with different shapes. First, the metasurfaces shown in Figure 4 are intrinsically polarization insensitive, which is not the case for traditional metasurfaces with, e.g., elongated nanostructures. Second, since all the meta-atoms have the same dimensions, the design can be extremely dense, thus enhancing the device efficiency.

## 5. Conclusions

We have introduced a facile and cost-effective nanofabrication technique to produce Au<sub>*x*</sub>Ag<sub>1-*x*</sub> alloyed nanostructures with arbitrary stoichiometry solely determined by the thickness of the different deposited metals. Thanks to the low-temperature annealing process, well-alloyed nanostructures with arbitrary shape can be fabricated, including those with a high aspect ratio. This is not the case for conventional high-temperature annealing, in which nanostructures irreparably acquire an ill-defined blubbery geometry. Nanostructures fabricated with this technique retain their designed optical properties, as demonstrated with different systems, including Fano-resonant structures and metasurfaces built from a collection of similar nanostructures with different stoichiometries. The ellipsometric data of those alloys agree well with theoretical models. The successful fabrication of meta-holograms and meta-lenses demonstrates that this new fabrication technique unlocks additional degrees of freedom for the realization of advanced optical elements at the nanoscale.

## Supporting Information

Supporting Information is available from the Wiley Online Library or from the author.

## Acknowledgements

D.R. acknowledges the Swiss Government Excellence scholarship. Funding from the Swiss National Science Foundation (Project No. 200021\_162453) and from the European Research Council (No. ERC-2015-AdG-695206 Nanofactory) is gratefully acknowledged. The authors thank the staff of the EPFL MicroNanotechnology platform (CMi) for their support and Pierre Mettraux for XPS measurements.

Open access funding provided by Ecole Polytechnique Federale de Lausanne.

## Conflict of Interest

The authors declare no conflict of interest.

## Author Contributions

D.R. and H.-C.W. contributed equally to this work. D.R. and C.S. developed the low-temperature annealing process. D.R. fabricated all the nanostructures reported therein. H.-C.W. designed and measured the metasurfaces, performed the AFM measurements and explored the low-temperature alloying of other compounds. J.K. measured the spectral response of the nanostructures and analyzed their Fano resonances with the ECO model. All authors analyzed the results and contributed to the manuscript.

## Data Availability Statement

The data that support the findings of this study are openly available in Zenodo at <https://doi.org/10.5281/zenodo.5792966>, reference [58].

Received: October 13, 2021

Revised: February 2, 2022

Published online:

- [1] M. Fichtner, *Adv. Eng. Mater.* **2005**, *7*, 443.
- [2] J. Lu, Z. Chen, Z. Ma, F. Pan, L. A. Curtiss, K. Amine, *Nat. Nanotechnol.* **2016**, *11*, 1031.
- [3] M. R. Hartings, Z. Ahmed, *Nat. Rev. Chem.* **2019**, *3*, 305.
- [4] S. Burgener, S. Luo, R. Mclean, T. E. Miller, T. J. Erb, *Nat. Catal.* **2020**, *3*, 186.
- [5] S. Goodnick, A. Korin, P. Krstic, P. Mascher, J. Preston, A. Zaslavsky, *Nanotechnology* **2010**, *21*, 130201.
- [6] Q. H. Wang, K. Kalantar-Zadeh, A. Kis, J. N. Coleman, M. S. Strano, *Nat. Nanotechnol.* **2012**, *7*, 699.
- [7] C. Liu, H. Chen, S. Wang, Q. i Liu, Y. u. G. Jiang, D. W. Zhang, M. Liu, P. Zhou, *Nat. Nanotechnol.* **2020**, *15*, 545.
- [8] E. Engel, A. Michiardi, M. Navarro, D. Lacroix, J. A. Planell, *Trends Biotechnol.* **2008**, *26*, 39.
- [9] G. Song, L. Cheng, Y. Chao, K. Yang, Z. Liu, *Adv. Mater.* **2017**, *29*, 1700996.
- [10] J. Weiss, P. Takhistov, D. J. McClements, *J. Food Sci.* **2006**, *71*, R107.
- [11] W. L. Barnes, A. Dereux, T. W. Ebbesen, *Nature* **2003**, *424*, 824.
- [12] K. Thyagarajan, C. Santschi, P. Langlet, O. J. F. Martin, *Adv. Opt. Mater.* **2016**, *4*, 871.
- [13] J. P. Kottmann, O. J. F. Martin, *Appl. Phys. B* **2001**, *B73*, 299.
- [14] P. R. West, S. Ishii, G. V. Naik, N. K. Emani, V. M. Shalaev, A. Boltasseva, *Laser Photonics Rev.* **2010**, *4*, 795.
- [15] U. Guler, J. C. Ndukaife, G. V. Naik, A. G. A. Nnanna, A. V. Kildishev, V. M. Shalaev, A. Boltasseva, *Nano Lett.* **2013**, *13*, 6078.
- [16] H. Shim, Z. Kuang, O. D. Miller, *Opt. Mater. Express* **2020**, *10*, 1561.
- [17] J. Zhang, Y. Tang, K. Lee, M. Ouyang, *Nature* **2010**, *466*, 91.
- [18] M. G. Blaber, M. D. Arnold, M. J. Ford, *J. Phys.: Condens. Matter* **2010**, *22*, 143201.
- [19] Y. Yang, Q. Zhang, Z.-W. Fu, D. Qin, *ACS Appl. Mater. Interfaces* **2014**, *6*, 3750.
- [20] J. Feng, C. Gao, Y. Yin, *Nanoscale* **2018**, *10*, 20492.
- [21] D. E. Gheorghie, L. Cui, C. Karmonik, A. Brazdeikis, J. M. Penalzoa, J. K. Young, R. A. Drezek, M. Bikram, *Nanoscale Res. Lett.* **2011**, *6*, 554.
- [22] C. Gao, Y. Hu, M. Wang, M. Chi, Y. Yin, *J. Am. Chem. Soc.* **2014**, *136*, 7474.
- [23] C. Gong, A. Kaplan, Z. A. Benson, D. R. Baker, J. P. McClure, A. R. Rocha, M. S. Leite, *Adv. Opt. Mater.* **2018**, *6*, 1800218.
- [24] M. Park, C. S. H. Hwang, K.-H. Jeong, *ACS Appl. Mater. Interfaces* **2018**, *10*, 290.
- [25] Y. Sanguansap, K. Karn-Orachai, R. Laocharoensuk, *Appl. Surf. Sci.* **2020**, *500*, 144049.
- [26] M. Kahraman, E. R. Mullen, A. Korkmaz, S. Wachsmann-Hogiu, *Nanophotonics* **2017**, *6*, 831.
- [27] S. Patskovsky, E. Bergeron, D. Rioux, M. Simard, M. Meunier, *Analyst* **2014**, *139*, 5247.
- [28] S.-Y. Tseng, S.-Y. Li, S.-Y. Yi, A. Y. Sun, D.-Y. Gao, D. Wan, *ACS Appl. Mater. Interfaces* **2017**, *9*, 17306.
- [29] P. Wang, Y. Bai, C. Yao, X. Li, L. Zhou, W. Wang, A. M. El-Toni, J. Zi, D. Zhao, L. Shi, F. Zhang, *Anal. Chem.* **2017**, *89*, 2583.
- [30] G. Qiu, S. P. Ng, C.-M. L. Wu, *Sens. Actuators, B* **2018**, *265*, 459.
- [31] S. Chattopadhyay, S. Bysakh, P. M. Mishra, G. De, *Langmuir* **2019**, *35*, 14364.
- [32] R. Kavitha, S. G. Kumar, *Chem. Pap.* **2020**, *74*, 717.
- [33] H. An, M. Li, R. Liu, Z. Gao, Z. Yin, *Chem. Eng. J.* **2020**, *382*, 122953.
- [34] C. S. H. Hwang, M.-S. Ahn, Y. Lee, T. Chung, K.-H. Jeong, *Sci. Rep.* **2019**, *9*, 9082.
- [35] M. Valenti, A. Venugopal, D. Tordera, M. P. Jonsson, G. Biskos, A. Schmidt-Ott, W. A. Smith, *ACS Photonics* **2017**, *4*, 1146.
- [36] W. P. Davey, *Phys. Rev.* **1925**, *25*, 753.
- [37] G. Guisbiers, R. Mendoza-Cruz, L. Bazán-Díaz, J. J. Velázquez-Salazar, R. Mendoza-Perez, J. A. Robledo-Torres, J.-L. Rodríguez-Lopez, J. M. Montejano-Carrizales, R. L. Whetten, M. José-Yacamán, *ACS Nano* **2016**, *10*, 188.
- [38] I. Lee, S. W. Han, K. Kim, *Chem. Commun.* **2001**, 1782.
- [39] R. Ferrando, J. Jellinek, R. L. Johnston, *Chem. Rev.* **2008**, *108*, 845.
- [40] K. D. Gilroy, A. Ruditskiy, H.-C. Peng, D. Qin, Y. Xia, *Chem. Rev.* **2016**, *116*, 10414.
- [41] H. T. Beyene, V. S. K. Chakravadhanula, C. Hanisch, M. Elbahri, T. Strunskus, V. Zaporojtchenko, L. Kienle, F. Faupel, *J. Mater. Sci.* **2010**, *45*, 5865.
- [42] C. Gong, M. R. S. Dias, G. C. Wessler, J. A. Taillon, L. G. Salamanca-Riba, M. S. Leite, *Adv. Opt. Mater.* **2017**, *5*, 1600568.
- [43] W. Albrecht, J. E. S. Van Der Hoeven, T.-S. Deng, P. E. De Jongh, A. Van Blaaderen, *Nanoscale* **2017**, *9*, 2845.
- [44] K. Liu, Y. Bai, L. Zhang, Z. Yang, Q. Fan, H. Zheng, Y. Yin, C. Gao, *Nano Lett.* **2016**, *16*, 3675.
- [45] T. Zhang, F. Zhou, L. Hang, Y. Sun, D. Liu, H. Li, G. Liu, X. Lyu, C. Li, W. Cai, Y. Li, *J. Mater. Chem. C* **2017**, *5*, 11039.
- [46] M. S. Shore, J. Wang, A. C. Johnston-Peck, A. L. Oldenburg, J. B. Tracy, *Small* **2011**, *7*, 230.
- [47] Y. Chen, *Microelectron. Eng.* **2015**, *135*, 57.
- [48] Y. Nishijima, S. Akiyama, *Opt. Mater. Express* **2012**, *2*, 1226.
- [49] L. Xu, L. S. Tan, M. H. Hong, *Appl. Opt.* **2011**, *50*, G74.
- [50] Y. Bai, C. Gao, Y. Yin, *Nanoscale* **2017**, *9*, 14875.
- [51] X. Wang, C. Santschi, O. J. F. Martin, *Small* **2017**, *13*, 1700044.
- [52] J. Lapujoulade, *Surf. Sci. Rep.* **1994**, *20*, 195.
- [53] S. Kakhodazadeh, F. A. A. Nugroho, C. Langhammer, M. Beleggia, J. B. Wagner, *ACS Photonics* **2019**, *6*, 779.
- [54] J.-S. Huang, V. Callegari, P. Geisler, C. Brüning, J. Kern, J. C. Prangma, X. Wu, T. Feichtner, J. Ziegler, P. Weinmann, M. Kamp, A. Forchel, P. Biagioni, U. Sennhauser, B. Hecht, *Nat. Commun.* **2010**, *1*, 150.
- [55] P.-T. Shen, Y. Sivan, C.-W. Lin, H.-L. Liu, C.-W. Chang, S.-W. Chu, *Opt. Express* **2016**, *24*, 19254.
- [56] D. Rioux, S. Vallières, S. Besner, P. Muñoz, E. Mazur, M. Meunier, *Adv. Opt. Mater.* **2014**, *2*, 176.
- [57] O. Peña-Rodríguez, M. Caro, A. Rivera, J. Olivares, J. M. Perlado, A. Caro, *Opt. Mater. Express* **2014**, *4*, 403.
- [58] D. Ray, H.-C. Wang, J. Kim, C. Santschi, O. J. F. Martin, <https://doi.org/10.5281/zenodo.5792966> (Zenodo), **2021**.
- [59] A. M. Kern, A. J. Meixner, O. J. F. Martin, *ACS Nano* **2012**, *6*, 9828.
- [60] M. Argyle, C. Bartholomew, *Catalysts* **2015**, *5*, 145.
- [61] J. P. Kottmann, O. J. F. Martin, D. R. Smith, S. Schultz, *Chem. Phys. Lett.* **2001**, *341*, 1.
- [62] A. Lovera, B. Gallinet, P. Nordlander, O. J. F. Martin, *ACS Nano* **2013**, *7*, 4527.
- [63] A. M. Kern, O. J. F. Martin, *J. Opt. Soc. Am. A* **2009**, *26*, 732.
- [64] B. Gallinet, A. M. Kern, O. J. F. Martin, *J. Opt. Soc. Am. A* **2010**, *27*, 2261.
- [65] M. Thangamuthu, C. Santschi, O. J. F. Martin, *Thin Solid Films* **2020**, *709*, 138195.
- [66] H.-C. Wang, C. H. Chu, P. C. Wu, H.-H. Hsiao, H. J. Wu, J.-W. Chen, W. H. Lee, Y.-C. Lai, Y.-W. Huang, M. L. Tseng, S.-W. Chang, D. P. Tsai, *Small* **2018**, *14*, 1703920.
- [67] D. K. Gramotnev, S. I. Bozhevolnyi, *Nat. Photonics* **2010**, *4*, 83.
- [68] G. Lévêque, O. J. F. Martin, *Opt. Express* **2006**, *14*, 9971.



- [69] F. Ding, A. Pors, S. I. Bozhevolnyi, *Rep. Prog. Phys.* **2017**, *81*, 026401.
- [70] L. Gao, F. Lemarchand, M. Lequime, *J. Eur. Opt. Soc. Rapid Publ.* **2013**, *8*, 1301.
- [71] Y. Z. Ho, B. H. Cheng, W.-L. Hsu, C.-M. Wang, D. P. Tsai, *Appl. Phys. Express* **2016**, *9*, 072502.
- [72] Y.-W. Huang, W. T. Chen, W.-Y. Tsai, P. C. Wu, C.-M. Wang, G. Sun, D. P. Tsai, *Nano Lett.* **2015**, *15*, 3122.
- [73] S. Wang, P. C. Wu, V.-C. Su, Y.-C. Lai, C. Hung Chu, J.-W. Chen, S.-H. Lu, J. Chen, B. Xu, C.-H. Kuan, T. Li, S. Zhu, D. P. Tsai, *Nat. Commun.* **2017**, *8*, 187.